J Nanostruct 16(3): 3473-3483, Summer 2026

RESEARCH PAPER

Synthesis and Plasma spectra characterization of Au, CeO_2 Nanoparticles using Pulsed Laser Deposition

Ruqaya Talib Kadhim [1], Ibtihaj Hussein Ali [2], Huda O. Saheb [3]*

[1] *Ministry of Education, General Directorate for Education in Thi-Qar, Iraq*

[2] *Ministry of Education, General Directorate for Education in Al-Qadisiyah, Iraq*

[3] *College of Science, University of Sumer, Iraq*

ARTICLE INFO

Article History:
Received 03 March 2026
Accepted 19 May 2026
Published 01 July 2026

Keywords:
Cerium oxide (CeO_2) nanoparticles
Gold (Au)
Plasma Spectroscopic
Pulsed Laser Deposition PLD

ABSTRACT

This study investigates the synthesis and plasma energy characterization of gold (Au) and cerium oxide (CeO_2) nanoparticles via pulsed laser deposition (PLD), with a focus on optimizing their structural and functional properties for biosensing applications. The conditions for the controlled fabrication of Au-CeO_2 nanoparticles by laser ablation were optimized (KrF 248 nm excimer laser, fluence: 2-10 J/cm^2) and the dynamics of the plasma was investigated by optical emission spectroscopy (OES) and quadrupole mass spectrometry (QMS). The correlation between the key plasma parameters such as electron temperature (T_e = 1–2.6 eV) and density ($n_e = 10^{16}$–10^{18} cm^{-3}) with laser energy was reported, where the higher energy the larger the intensities of the spectral lines and the plasma shielding effects. Au nanoparticles (14.4 nm crystallite size) and CeO_2 (27 nm particle size) were found to have face centered cubic (FCC) and cubic fluorite structures, respectively, with preferential orientation along the (111) plane, respectively, according to X-ray diffraction (XRD). The uniform morphologies were confirmed with field emission scanning electron microscopy (FE-SEM).

How to cite this article
Kadhim R., Ali I., O. Saheb H. Synthesis and Plasma spectra characterization of Au, CeO_2 Nanoparticles using Pulsed Laser Deposition. J Nanostruct, 2026; 16(3):3473-3483. DOI: 10.22052/JNS.2026.03.039

INTRODUCTION

In recent years, the synthesis and application of hybrid nanoparticles have attracted considerable interest in advanced technological applications because of their unique physicochemical properties [1] which makes them suitable for catalysis, energy storage, biosensing and other fields. Of these, the Au-CeO_2 nanoparticles are particularly promising because of their excellent catalytic activity (oxygen vacancy-mediated redox activity of Ce^{3+}/Ce^{4+} sites), biocompatibility, and localized surface plasmon resonance (LSPR) in the range of visible-NIR (500–800 nm), which is highly advantageous for biosensor development [1, 2]. Fabrication of high purity nanostructured thin films and nanoparticles with control of composition and morphology by Pulsed Laser Deposition (PLD) has proven to be a versatile technique for the transfer of complex materials in the required amount and at relatively low substrate temperatures (ranging down to 300°C) [3-5]. The structural (crystallite size, defect density) and functional (plasmonic absorption, catalytic turnover frequency) properties of Au-

* *Corresponding Author Email: Ruqayatalib2025@gmail.com*

CeO_2 nanoparticles seeded by PLD are, however, not yet fully explored, especially in biosensing applications [6,7]. The main objectives of this study are to optimize the Au-CeO_2 nanoparticles synthesized by the PLD method, in order to study the optical and catalytic properties of the plasma energy parameters (time-resolved optical emission spectroscopy, quadrupole mass spectrometry) [8] and optimize their optical properties (LSPR peak position and FWHM) and catalytic properties (CO oxidation activity at temperatures ≤100°C). These nanoparticles can be used as biosensing platforms, and we seek to improve their performance by systematically investigating the interplay between the laser ablation conditions (laser fluence: 2–10 J/cm²; wavelength: 248 nm KrF excimer), the characteristics of the plasma plumes (plume expansion velocity: 105–106 cm/s), and the formation of nanoparticles (Au nanoparticle size distribution: 5–30 nm; CeO2 lattice parameter shifts via XRD). The optimized Au-CeO_2 nanostructures are then assessed with respect to their sensitivity (H_2O_2 detection limit ≤100 pM), selectivity (<5% interference from ascorbic acid/uric acid) and stability (signal loss ≤10% after 30 days), which further opens the door for next generation biosensors with higher efficiency and reliability [10].

MATERIALS AND METHODS

Substrate Preparation

To achieve a contaminant free surface, the glass substrates (SiO_2 25 × 25 mm) must be cleaned thoroughly in order to start the deposition process. The slides are ultrasonicated in absolute ethanol (99.9%) for a period of 15 minutes to wash away organic contaminates, and then washed with deionized water to remove any traces of the solvents and particles. Then the substrates are dried with high purity N_2 gas to avoid water spot or water streak. The cleaned substrates are then plasma-treated in O_2 environment (50 W, 5 min) to further enhance the adhesion of the deposited nanoparticles. This step will generate a hydrophilic surface with active sites that will encourage more bonding between the substrate and the deposited Au-CeO_2 nanostructures.

Substrate Preparation

High purity (Au 99.99% and Ce 99.99%) metallic targets for ablation are needed for the PLD process and are available as sheets (Kurt J. Lesker). The targets are placed on a rotating mount so that they are ablated evenly and there is no localized crater formation, in order to prevent inconsistent deposition rates. The Ce target is pre-ablated in a low pressure O_2 gas environment (10mTorr) to get CeO_2 (which is the desired film) in the final product. This process is used to create a thin oxide layer on the target surface to facilitate deposition of stoichiometric CeO_2 instead of Ce metal or sub-oxides in the main ablation process.

PLD System Configuration

The deposition process is performed on a specially constructed PLD system including several

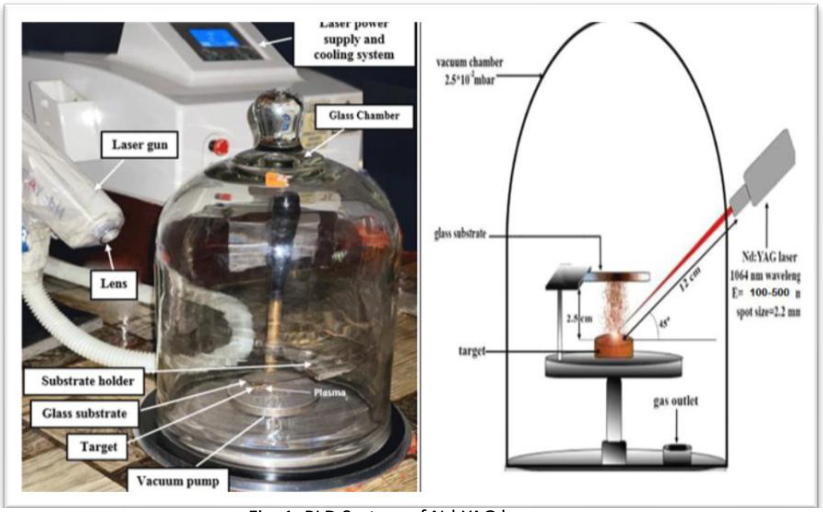

Fig. 1. PLD System of Nd:YAG laser.

important parts, such as laser source A, which is a Q-switched Nd:YAG laser (Model HF-301, Huafei Technology, China), playing a role of providing high energy pulses for ablating the target. Output: Fundamental or frequency-doubled (1064 nm) depending on the absorption characteristics required in the target material. Pulse duration: 6-8 nanoseconds, which helps to keep material ejected without major thermal diffusion. Repetition rate: 10Hz (enables controlled deposition with a reduction of heat accumulation). Laser fluence: Can be varied between 2 and 5 J/cm2 to optimize the ablation for achieving quality nanoparticles and a desired ablation rate, depending on the material, as illustrated in Fig. 1.

Optical Setup

Laser beam is focused by convex lens of 100 mm focal length on the target by setting the incidence angle at 45° for efficient energy coupling with the target and minimum back-reflection.

Vacuum Chamber

Residual gas contamination is minimized by vacuuming the chamber with a turbomolecular pump down to a base pressure of 1×10^{-6} Torr.

The background gas (Ar for Au, O_2 for CeO_2) is fed in during deposition at controlled pressures (50-100 mTorr) to control plasma dynamics and properties of the film.

Substrate Holder

The holder is then heated to 300-500°C (controlled by thermocouple) to increase crystallinity and bonding of the films deposited.

The substrates are placed 5 cm away from the target, which distance is the optimum to ensure the uniform deposition and the control of the nanoparticles size.

The deposition of nanoparticles Process involves the process of them settling on the water's surface.

The gold (Au) and cerium (Ce) metal targets are first ablated for 5 minutes under vacuum before the actual deposition. This initial ablation process is important to remove surface oxides, adsorbed contaminants and other impurities that could affect the quality of the deposited films. In this stage, the laser beam continually scans the surface of the target, which ensures the area to be ablated clean and uniform, thereby facilitating uniform nanoparticle growth.

Five different energy levels of the laser pulse were used to investigate the influence of the energy input on the synthesis process: 50 mJ, 100 mJ, 150 mJ, 200 mJ and 250 mJ. The effects of these incremental energy levels on the formation of plasma, particle size, and deposition rate were analyzed in detail.

Au nanoparticle deposition is performed in high purity Ar (99.999%) gas at 50 mTorr. The inert Ar gas also prevents the plasma plume from oxidizing the material, increasing the efficiency of the nucleation and reducing the amount of unwanted oxidation. The total fluence of 5000 pulses is applied with a fluence of 3 J/cm², to produce ultrasmall gold nanoparticles (~10 nm) with a narrow size distribution. The low oxygen situation helps to maintain the plasmonic property of Au without the risk of oxidation.

The growth of ceria (CeO_2), by contrast, needs an oxygen rich environment. High purity oxygen (99.999%) is used to fill the deposition chamber at 100 mTorr to ensure the formation of a stoichiometric CeO_2 phase and prevent the appearance of sub-oxide phases like Ce_2O_3. The bonding in Ce–O is strong, and the laser fluence of 4 J/cm² and 10,000 laser pulses are used to obtain a ~50 nm thick CeO_2 layer with controlled crystallinity. The pressure of oxygen gas is carefully controlled to balance the oxidation and deposition rates.

The synthesized Au–CeO_2 nanostructures are then thermally treated in air at 400°C for 1 hour. This post deposition annealing increases the crystallinity of CeO_2 by decreasing the lattice defects and the stable fluorite crystal structure (Fm-3m space group). Besides, thermal treatment enhances the bonding between Au and CeO_2, which is crucial for the efficient charge transfer process in catalytic and biosensing applications.

RESULTS AND DISCUSSION

The spectra of Au,Ce targets

Two different samples of pure Cerium Oxide (CeO_2) and pure Gold (Au) were investigated using optical emission spectroscopy (OES) obtained from a 1064 nm nanosecond Nd:YAG laser, to characterize the plasma plume created. The experiments performed on laser induced plasma were performed at atmospheric pressure which is a common condition for such applications. The present study was focused on the effect of the laser energy and wavelength on the plasma properties.

We took the emission spectra at different energies of the laser pulse from 200 mJ to 800 mJ and noticed a consistent trend in plasma signal with respect to laser pulse energy. The emitted light from the plasma plume was collected and analysed using an optical fiber bundle connected to a spectrometer. The detailed information regarding the elemental composition of the samples was obtained from the spectral emissions that occurred after the excited species in the plasma relaxed. Elucidation of the emission spectra of cerium and gold plamas showed characteristic lines which can be used to identify pure elements and oxides in the material. When an electron in the excited state returns to a lower energy level or the ground state it releases a photon with a specific wavelength, creating a spectral line emission. In addition, continuum radiation, namely Bremsstrahlung radiation (free-free transitions) and recombination radiation (free-bound transitions) were observed. The analysis of

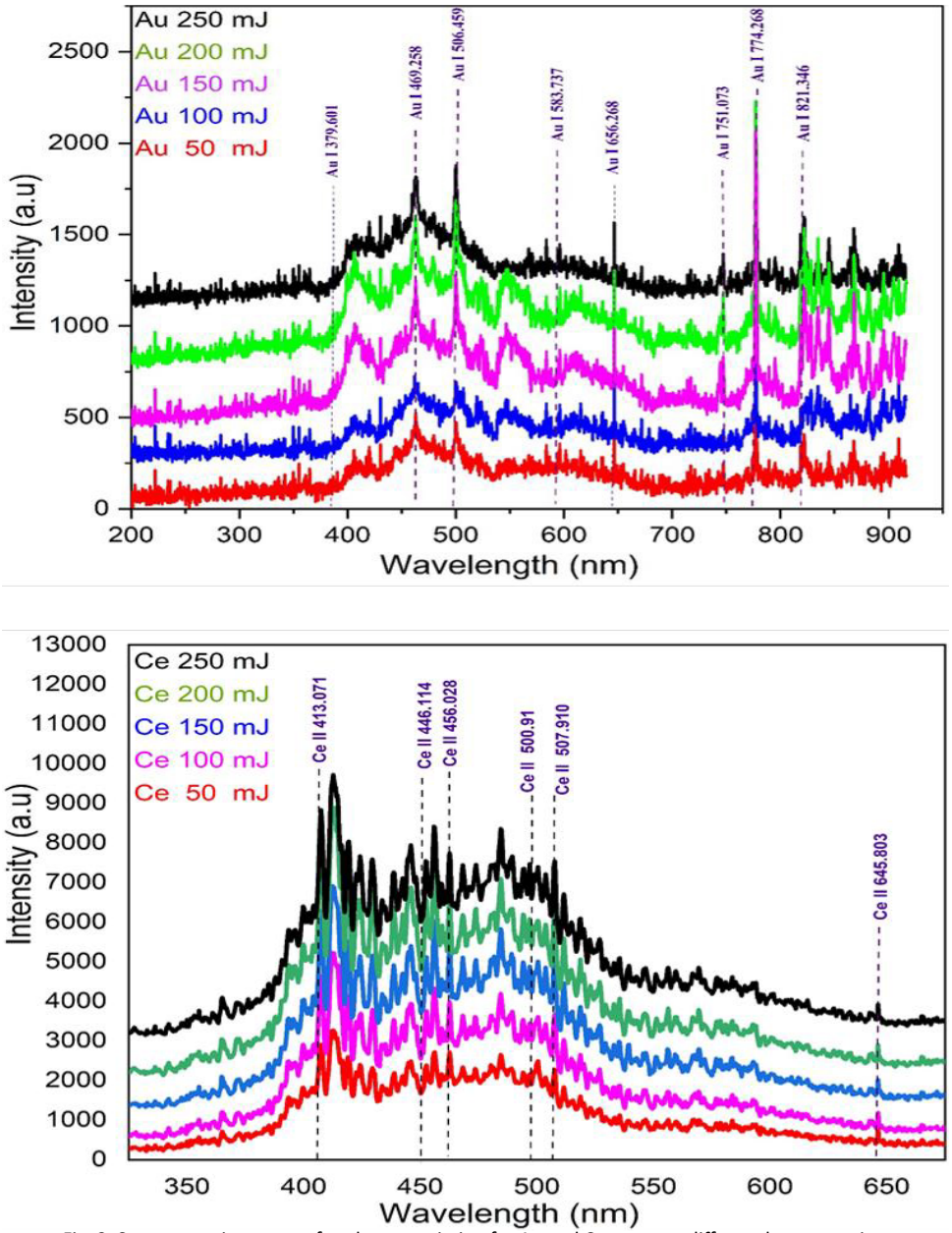

Fig. 2. Spectroscopic patterns for plasma emission for Au and Ce target at different laser energies.

gold plasma showed very clear emission peaks when the plasma was excited with different pulse energies of the 1064 nm laser, across the entire spectral range from 200 nm to 700 nm, as shown in Fig. 2. These emission lines were found to be stronger with higher laser peak energies. This increase is due to the increase of mass ablation rate from the target, thus increasing the number of excited and ionized atoms. This leads to higher absorption of laser energy by the plasma and higher intensities of the plasma emission lines, suggesting a direct link between the energy of the laser, the energy of the plasma, and the emission line intensity [11].

Plasma created when laser pulses interact with the material of the target contains neutral atoms, electromagnetic radiation, excited-state electrons and ions as well. This radiation is emitted by the resulting plasma, and can be analyzed using the plasma emission spectrum (usually graphed as intensity vs. wavelength). The emission spectrum of the plasma that was generated by the target made of gold, with the irradiation of the target with Q-switched Nd:YAG laser pulses, is shown in Fig. 3, as a function of the peak energy of the laser pulse in the DDW. The spectrum was

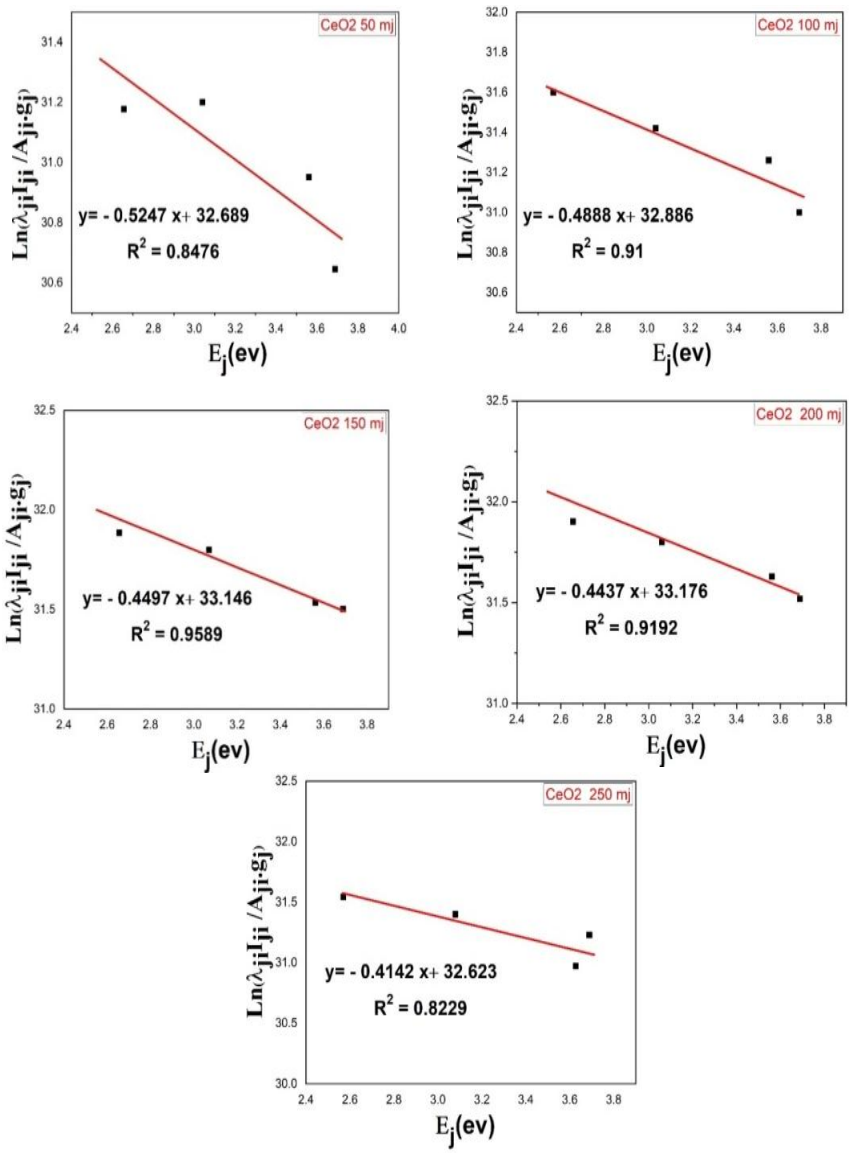

Fig. 3. Boltzmann plot for plasma emission Ce II target at different laser energy.

obtained by optical emission spectroscopy (OES) and contain spectral emission for gold, silver and zirconium. Many different spectral lines, corresponding to the transitions of atoms in the 200–900 nm range, are observed in the spectra. This is evident from figure which shows that the peak energy of the laser has a significant influence on the strength of the emission lines. The larger the laser energy, the greater is the mass ablation rate of the target material, and hence the number of excited and ionized atoms. This in turn improves the absorption of the plasma and the strength of the spectral lines emitted. Likewise, the plasma properties generated by the laser were examined for the case of silver and zirconium targets. The results clearly show a consistent trend, and again confirmed the strong dependence of the plasma emission properties on the laser peak energy.

Electron Temperature Determination for Metal Targets

The electron temperature (T_e) was calculated

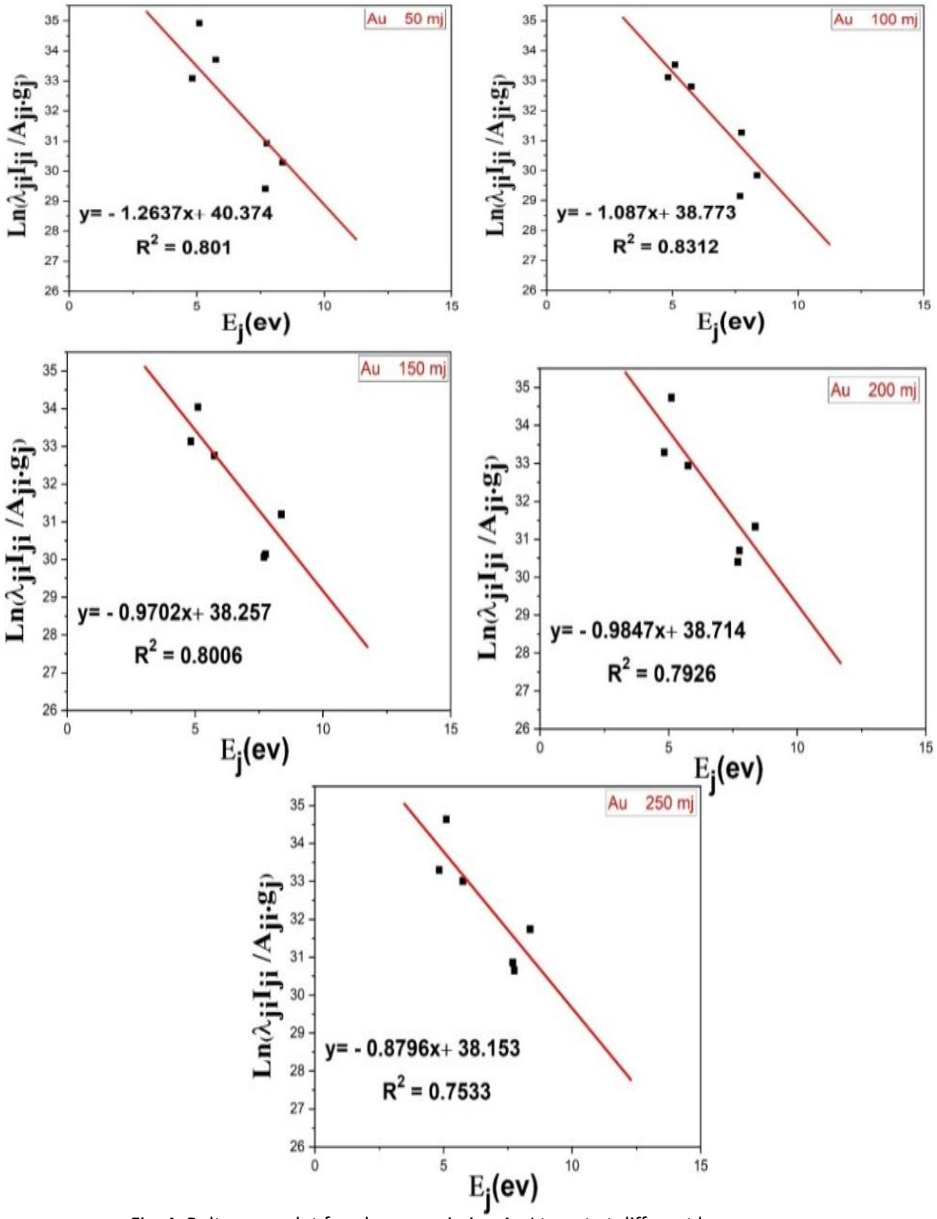

Fig. 4. Boltzmann plot for plasma emission Au I target at different laser energy.

using the inverse of the slope obtained from the best-fit line in the Boltzmann plot, as described by Eq. 1:

$$I_{ji} = \frac{N(T)}{U(T)} \; g_j \, A_{ji} \, \frac{hc}{\lambda_{ji}} \; e^{-\frac{E_j}{K_\beta T_e}} \qquad (1)$$

Requirements for the boltzmann plot method is that the emission lines are from the same species and ionization stage [12]. In this analysis, six spectral lines of neutral gold (Au I) were selected at the following wavelengths: 379.601 nm, 469.258 nm, 506.459 nm, 583.737 nm, 627.817 nm, and 751.073 nm. The coefficient of determination (R^2) values and the associated fitting equations are given in Fig. 3. Similarly, the characteristics of the laser induced plasma was investigated for cerium target as found in the Fig. 4 such that the R2 values of the obtained fit were between 0.75 – 0.83, which is quite good but not in the ideal range of perfect correlation.

Electron densities of the target

The electron densities (n_e) were calculated using the Stark broadening method, as described by Equation [13]:

$$n_e(cm^{-3}) = \left[\frac{\Delta\lambda}{2\omega_s}\right] N_r \qquad (2)$$

and shown in Fig. 5. In plasma, the broadening and shifting of spectral lines are greatly affected by collisions with charged particles (like electrons and ions). The phenomenon is called Stark broadening,

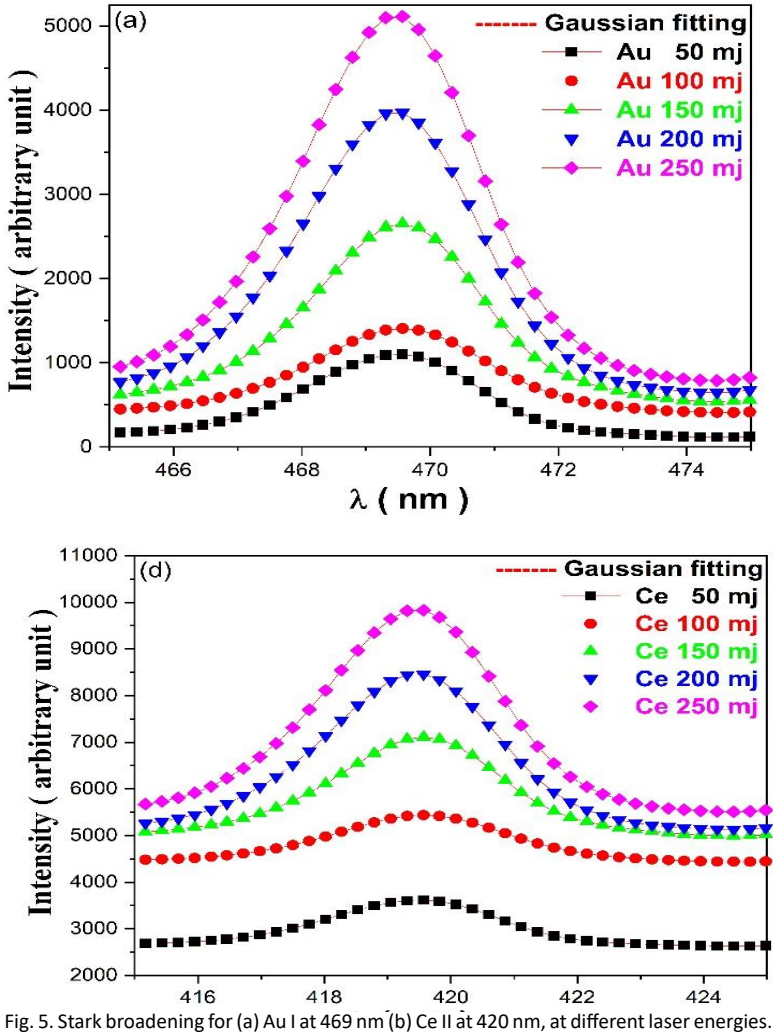

Fig. 5. Stark broadening for (a) Au I at 469 nm (b) Ce II at 420 nm, at different laser energies.

and the broadening of the line and the shift of the peak wavelength can be measured and it is possible to estimate the electron density.

The electron density (n_e) increases as the laser pulse energy increases as can be seen in Fig. 6. This is because the formation of a dense plasma becomes opaque to the incident laser beam, thus protecting the target material at higher energy levels. Thus the laser energy is absorbed by the plasma (plasma absorption) instead of directly

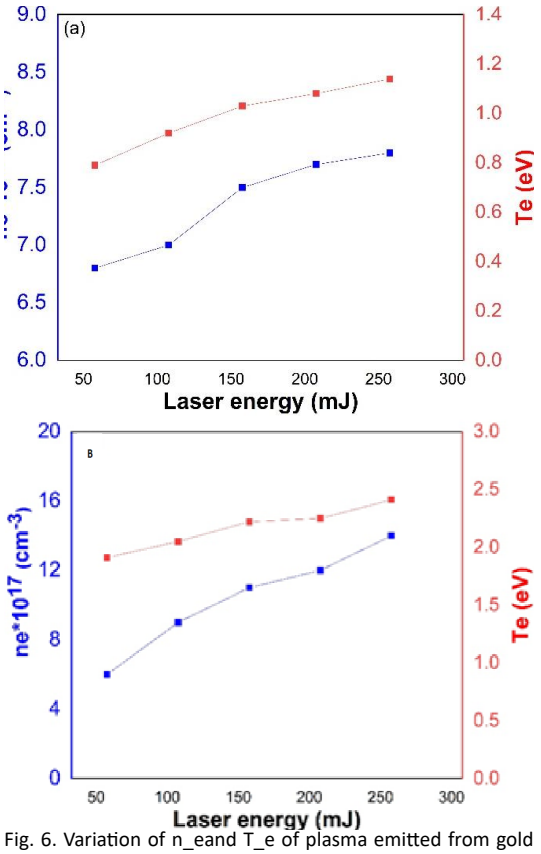

Fig. 6. Variation of n_eand T_e of plasma emitted from gold and cerium targets respectively at different laser energies.

Table 1 plasma parameters calculated from spectroscopic lines for different metals in the air using 1064 nm laser, with different laser energies.

Metals	E (mJ)	T_e (eV)	$n_e \times 10^{17}$ (cm^{-3})	$\omega_{pe} \times 10^{13}$ (rad/sec)	$\lambda_D \times 10^{-6}$ (cm)	N_D	$f_p \times 10^{12}$ (Hz)
Au	50	1.19	6	4.37	1	2.9	7
	100	1.21	6.8	4.63	0.99	2.8	7.4
	150	1.23	9	5.35	0.87	2.5	8.5
	200	1.25	11	5.98	0.78	2.3	9.5
	250	1.26	11	6.04	0.78	2.3	9.6
Ce	50	1.91	6	4.37	1.3	5.8	7
	100	2.05	9	5.35	1.1	5.3	8.5
	150	2.22	11	5.78	1.1	5.6	9.2
	200	2.25	12	6.18	1	5.3	9.8
	250	2.41	14	6.55	0.99	5.6	10

interacting with the surface of the target. The electron temperature (T_e) is almost constant at higher laser peak energies, which is a saturation effect. This decrease in the amount of laser energy transmitted through the plasma is called plasma shielding because the plasma created along the way reduces the intensity of the laser beam and thus the amount of energy deposited.

Plasma parameters results

As presented in Table 1, the key plasma parameters—namely electron temperature (T_e), electron density (n_e), Debye length (λ_D), Debye sphere number (N_D), electron plasma frequency

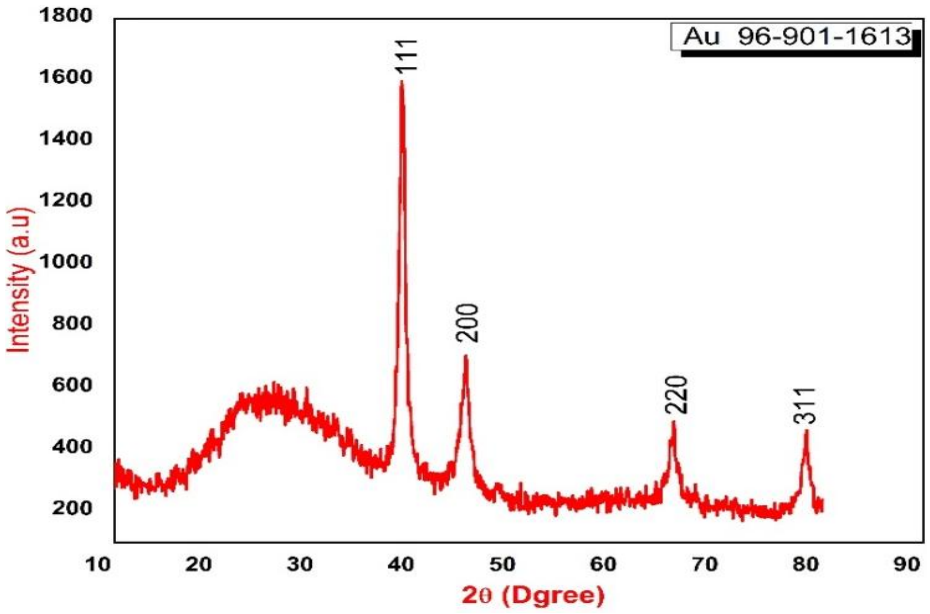

Fig. 7. XRD patterns of Au thin film.

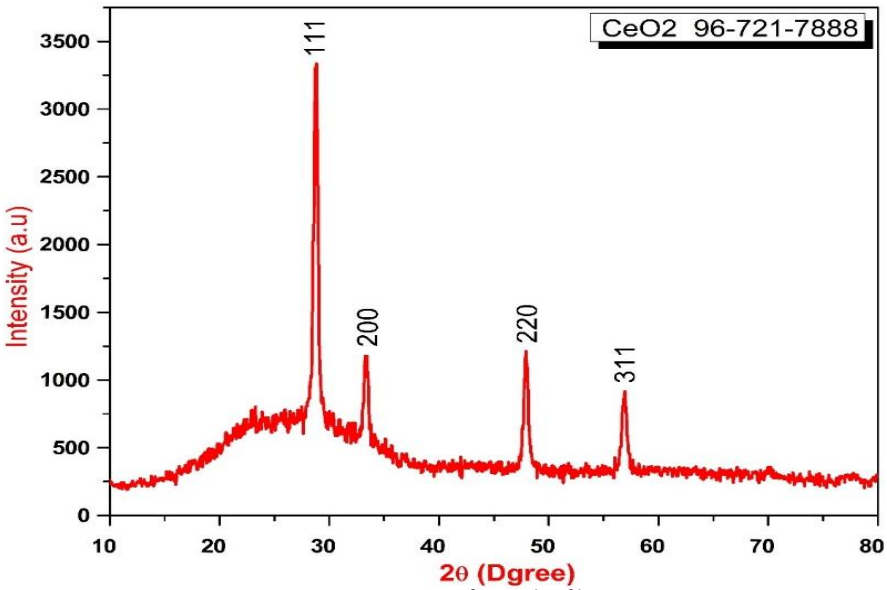

Fig. 8. XRD patterns of CeO_2 thin film.

(ω_{pe}), and plasma frequency (f_p) [14].

$$f_{pe} = \frac{\omega_{pe}}{2\pi} \approx 8.98\sqrt{n_e} \quad (Hz) \tag{3}$$

were evaluated for Au, Ag, Zr, and Ce targets under varying laser energy conditions. A detailed summary of the computed values for Debye length (λ_D) and plasma frequency (f_p) is provided in Table 1. The findings reveal that plasma frequency increases with laser energy, which is directly associated with the corresponding rise in electron density (n_e).

XRD Analysis

The X-ray diffraction (XRD) pattern of Gold NPs synthesized is shown in Fig. 7, which shows four prominent and sharp diffraction peaks at 38.43°, 44.73°, 65.23°, and 78.33° (2θ). The peaks confirm the presence of pure gold nanoparticles of crystalline form. Lattice planes (111), (200), (220) and (311) are identified in the powder pattern, which corresponds to the diffraction planes of face centred cubic (FCC) structure as seen on the standard JCPDS card No. 96-901-1613. The average size of the crystallites of the gold nanoparticles was estimated to be about 14.4 nm, which was obtained from Scherrer's equation [15].

The XRD pattern is accompanied by a detailed summary of the observed diffraction planes and the peak positions that correspond to each diffraction plane. The synthesized CeO_2

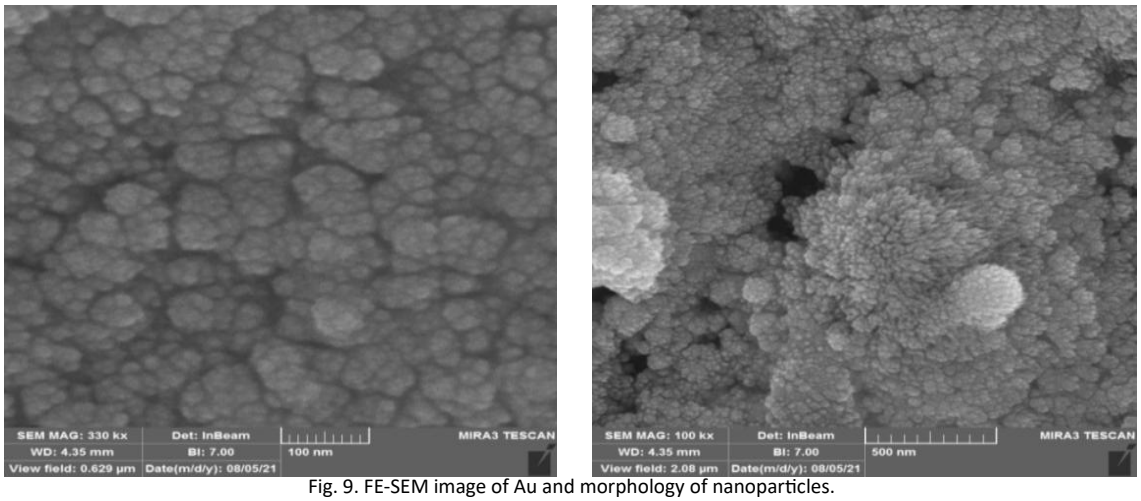

Fig. 9. FE-SEM image of Au and morphology of nanoparticles.

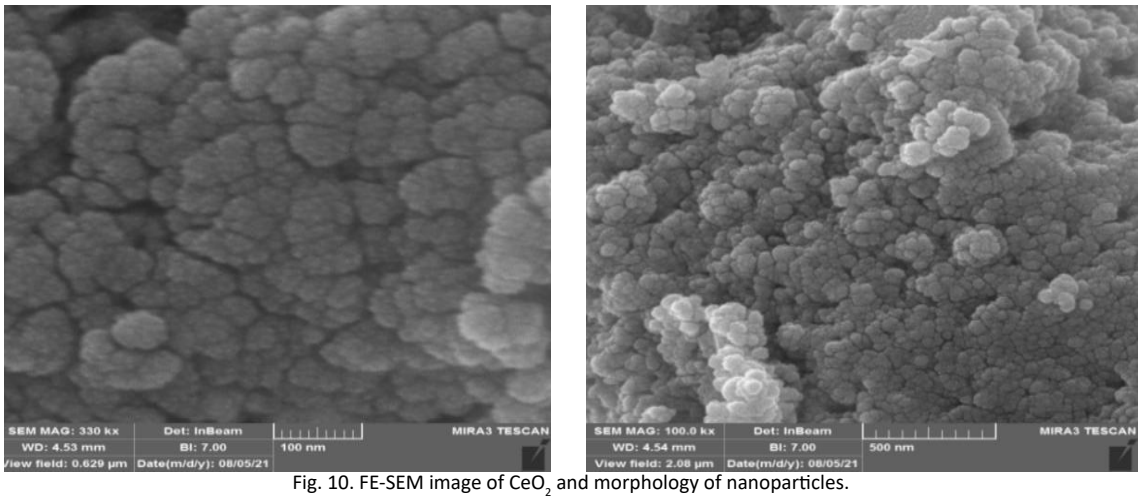

Fig. 10. FE-SEM image of CeO_2 and morphology of nanoparticles.

nanoparticles are characterized by XRD pattern as shown in Fig. 8, which shows the presence of four strong diffraction peaks at 2θ angles of 28.78°, 33.36°, 47.95°, and 56.91° indicating the crystallographic planes (111), (200), (220), and (311) respectively.

The peaks agree with the reference CeO_2 (JCPDS No. 96-721-7888) which indicates the formation of a cubic structure for CeO2. Notably, the (111) plane at 28.78° is much more intense than the other diffraction peaks, which may indicate preferential crystallographic orientation or increased crystallinity along this lattice plane. Further confirmation of successful synthesis of CeO_2 nanoparticles is achieved through the calculation of crystallite size from the broadening of the peaks and alignment of the peaks with the reference pattern, giving a phase purity.

The morphological and crystallographic features of the synthesized Au and CeO_2 nanoparticles and their core–shell structures were examined using Field Emission Scanning Electron Microscopy (FE-SEM) at different magnifications. The FE-SEM image of gold nanoparticles (Fig. 9) shows the presence of particles with an average size of ~20 nm, displaying a very clear acicular morphology. Likewise, FE-SEM image of Cerium oxide nanoparticles (Fig. 10) reveals the top view morphology of the sample and an estimated particle size of 27 nm which suggests the formation of relatively uniform and well defined structures.

CONCLUSION

In this study, Au and CeO_2 nanoparticles were successfully synthesized by pulsed laser deposition (PLD) and the structural and functional properties of the nanoparticles were optimized for future biosensing applications. The plasma parameters calculated from the optical emission spectroscopy (OES) and quadrupole mass spectroscopy (QMS) results ranged from 1–2.6 eV of the electron temperature and 10^{16}–10^{18} cm^{-3} of the electron density with an increase of laser energy levels. The X-ray diffraction (XRD) results showed that both Au nanoparticles displayed a face-centered cubic (FCC) structure (~14.4 nm) together with CeO_2 nanoparticles that had a cubic fluorite structure (~27 nm). The results showed the formation of pure crystallines. The field emission scanning electron microscopy (FE-SEM) analysis revealed uniformity in morphology and size distribution in both the cases of the nanoparticles. The study indicates that the physical characteristics of nanoparticles can be accurately identified using managed PLD techniques, which proves that the technique has potential application to the development of biosensors that are highly selective and sensitive and can be more stable.

CONFLICT OF INTEREST

The authors declare that there is no conflict of interests regarding the publication of this manuscript.

REFERENCES

1. Dhaka A, Chand Mali S, Sharma S, Trivedi R. A review on biological synthesis of silver nanoparticles and their potential applications. Results in Chemistry. 2023;6:101108.
2. Zhang B, Zhang S, Liu B. Effect of oxygen vacancies on ceria catalyst for selective catalytic reduction of NO with NH3. Appl Surf Sci. 2020;529:147068.
3. Haider AJ, Alawsi T, Haider MJ, Taha BA, Marhoon HA. A comprehensive review on pulsed laser deposition technique to effective nanostructure production: trends and challenges. Optical and Quantum Electronics. 2022;54(8).
4. Krebs H-U, Weisheit M, Faupel J, Süske E, Scharf T, Fuhse C, et al. Pulsed Laser Deposition (PLD) -- A Versatile Thin Film Technique. Advances in Solid State Physics: Springer Berlin Heidelberg; 2003. p. 505-518.
5. Lamprou DA, Scoutaris N, Ross SA, Douroumis D. Polymeric Coatings and Their Fabrication for Medical Devices. Encyclopedia of Biomedical Engineering: Elsevier; 2019. p. 177-187.
6. Wang X, Zhang S, Cheng X, Zhu E, Hang W, Huang B. Ion kinetic energy distributions in laser-induced plasma. Spectrochimica Acta Part B: Atomic Spectroscopy. 2014;99:101-114.
7. Mostafa AM. The Influence of Various Parameters on the Ablation and Deposition Mechanisms in Pulsed Laser Deposition. Plasmonics. 2025;20(7):5627-5645.
8. Sortino AL, Censabella M, Munzi G, Boninelli S, Privitera V, Ruffino F. Laser-Based Synthesis of Au Nanoparticles for Optical Sensing of Glyphosate: A Preliminary Study. Micromachines. 2020;11(11):989.
9. Tański M, Barbucha R, Kocik M, Garasz K, Mizeraczyk J. Investigation of the laser generated ablation plasma plume dynamics and plasma plume sound wave dynamics. SPIE Proceedings; 2013/01/22: SPIE; 2013. p. 87030O.
10. Davidson E, Xi Z, Gao Z, Xia X. Ultrafast and sensitive colorimetric detection of ascorbic acid with Pd-Pt core-shell nanostructure as peroxidase mimic. Sensors International. 2020;1:100031.
11. Sun X, Wen J, Guo Q, Pang F, Chen Z, Luo Y, et al. Fluorescence properties and energy level structure of Ce-doped silica fiber materials. Optical Materials Express. 2017;7(3):751.
12. Abbass Q, Ahmed N, Ahmed R, Baig MA. A Comparative Study of Calibration Free Methods for the Elemental Analysis by Laser Induced Breakdown Spectroscopy. Plasma Chem Plasma Process. 2016;36(5):1287-1299.
13. Sadeghzadeh Lari E, Ranjbar Askari H, Meftah MT, Shariat M. Calculation of electron density and temperature of plasmas by using new Stark broadening formula of helium lines. Physics of Plasmas. 2019;26(2).
14. Chen Y, Zhao C, Pan Q, Zhang R, Gao Y, Li X, et al. Experimental Study on the Temporal Evolution Parameters of Laser–Produced Tin Plasma under Different Laser Pulse Energies for LPP–EUV Source. Photonics. 2023;10(12):1339.
15. Thamer AA, Hassani RH, Manaty OA. Synthesis of zinc oxide nanoparticles by eco-friendly method. AIP Conference Proceedings: AIP Publishing; 2025. p. 100003.